



## NRC Publications Archive Archives des publications du CNRC

### **Self-assembly formation of Bi-functional $\text{Co}_3\text{O}_4/\text{MnO}_2$ -CNTs hybrid catalysts for achieving both high energy/power density and cyclic ability of rechargeable zinc-air battery**

Xu, Nengneng; Liu, Yuyu; Zhang, Xia; Li, Xuemei; Li, Aijun; Qiao, Jinli; Zhang, Jiujun

This publication could be one of several versions: author's original, accepted manuscript or the publisher's version. / La version de cette publication peut être l'une des suivantes : la version prépublication de l'auteur, la version acceptée du manuscrit ou la version de l'éditeur.

For the publisher's version, please access the DOI link below. / Pour consulter la version de l'éditeur, utilisez le lien DOI ci-dessous.

#### **Publisher's version / Version de l'éditeur:**

<https://doi.org/10.1038/srep33590>

*Scientific Reports*, 6, pp. 33590-1-33590-10, 2016-09-20

#### **NRC Publications Record / Notice d'Archives des publications de CNRC:**

<https://nrc-publications.canada.ca/eng/view/object/?id=5be65895-4ca2-49b7-aeec-8f7a0733e29a>

<https://publications-cnrc.canada.ca/fra/voir/objet/?id=5be65895-4ca2-49b7-aeec-8f7a0733e29a>

Access and use of this website and the material on it are subject to the Terms and Conditions set forth at

<https://nrc-publications.canada.ca/eng/copyright>

READ THESE TERMS AND CONDITIONS CAREFULLY BEFORE USING THIS WEBSITE.

L'accès à ce site Web et l'utilisation de son contenu sont assujettis aux conditions présentées dans le site

<https://publications-cnrc.canada.ca/fra/droits>

LISEZ CES CONDITIONS ATTENTIVEMENT AVANT D'UTILISER CE SITE WEB.

#### **Questions?** Contact the NRC Publications Archive team at

PublicationsArchive-ArchivesPublications@nrc-cnrc.gc.ca. If you wish to email the authors directly, please see the first page of the publication for their contact information.

**Vous avez des questions?** Nous pouvons vous aider. Pour communiquer directement avec un auteur, consultez la première page de la revue dans laquelle son article a été publié afin de trouver ses coordonnées. Si vous n'arrivez pas à les repérer, communiquez avec nous à PublicationsArchive-ArchivesPublications@nrc-cnrc.gc.ca.



# SCIENTIFIC REPORTS



OPEN

## Self-assembly formation of Bi-functional $\text{Co}_3\text{O}_4/\text{MnO}_2$ -CNTs hybrid catalysts for achieving both high energy/power density and cyclic ability of rechargeable zinc-air battery

Nengneng Xu<sup>1,2</sup>, Yuyu Liu<sup>1</sup>, Xia Zhang<sup>2</sup>, Xuemei Li<sup>2</sup>, Aijun Li<sup>1</sup>, Jinli Qiao<sup>1,2</sup> & Jiujun Zhang<sup>1,3</sup>

$\alpha$ - $\text{MnO}_2$  nanotubes-supported  $\text{Co}_3\text{O}_4$  ( $\text{Co}_3\text{O}_4/\text{MnO}_2$ ) and its carbon nanotubes (CNTs)-hybrids ( $\text{Co}_3\text{O}_4/\text{MnO}_2$ -CNTs) have been successfully developed through a facile two-pot precipitation reaction and hydrothermal process, which exhibit the superior bi-functional catalytic activity for both ORR and OER. The high performance is believed to be induced by the hybrid effect among  $\text{MnO}_2$  nanotubes, hollow  $\text{Co}_3\text{O}_4$  and CNTs, which can produce a synergetic enhancement. When integrated into the practical primary and electrochemically rechargeable Zn-air batteries, such a hybrid catalyst can give a discharge peak power density as high as  $450 \text{ mW cm}^{-2}$ . At 1.0V of cell voltage, a current density of  $324 \text{ mA cm}^{-2}$  is achieved. This performance is superior to all reported non-precious metal catalysts in literature for zinc-air batteries and significantly outperforms the state-of-the-art platinum-based catalyst. Particularly, the rechargeable Zn-air battery can be fabricated into all-solid-state one through a simple solid-state approach, which exhibits an excellent peak power density of  $62 \text{ mW cm}^{-2}$ , and the charge and discharge potentials remain virtually unchanged during the overall cycles, which is comparable to the one with liquid electrolyte.

The increasing global energy usage, its associated fast fossil fuel depletion, and the resulted environmental concern have stimulated intensive research and development of clean and sustainable energy storage and conversion systems<sup>1–3</sup>. Among different energy storage and conversion options, electrochemical energy devices including batteries, fuel cells, and supercapacitors have been recognized as the most feasible and efficient ones. In the most recent years, the rechargeable metal–air batteries, which have a low fabrication cost, environmentally benign, and high safety, have received much interest because of their extremely higher energy density than any commercially available aqueous batteries and lithium-ion batteries<sup>4,5</sup>, making them one of the most promising candidates in energy storage and conversion, particularly for extending driving range of the next generation electric vehicles<sup>6–8</sup>. For example, Zinc-air batteries could achieve a specific energy density in excess of  $400 \text{ Wh kg}^{-1}$  ( $650 \text{ Wh L}^{-1}$ ) in a coin-cell configuration<sup>9–11</sup>. However, the electrically rechargeable Zn-air batteries face the challenge of sluggish kinetics of both oxygen reduction reaction (ORR) and  $\text{O}_2$  evolution reaction (OER) at the positive (cathode) electrode, which can lead to low round trip efficiency. In attempts to improve both the ORR and OER processes, carbon-supported precious metal-based bifunctional electrocatalysts such as Pt, Pd, Ag, Au, Ir and their alloys have been used to increase the rate of the reactions<sup>12–17</sup>. However, both these metals' high-cost/scarcity and insufficient stability make the technologies impracticable, particularly for a large-scale commercialization<sup>18</sup>. Therefore,

<sup>1</sup>Institute of Sustainable Energy, Shanghai University, 20 Chengzhong Road, Shanghai 201800, China. <sup>2</sup>College of Environmental Science and Engineering, Donghua University, 2999 Ren'min North Road, Shanghai 201620, China.

<sup>3</sup>Energy, Mining & Environment, National Research Council of Canada, Vancouver, BC, Canada. Correspondence and requests for materials should be addressed to A.L. (email: Aijun.li@shu.edu.cn) or J.Q. (email: qiaojl@dhu.edu.cn) or J.Z. (email: jiujun.zhang@shu.edu.cn)

developing non-precious metal-based materials such as metal oxides have become one of the important options for bi-functional catalysts for Zn-Air batteries.

Among different bi-functional catalysts explored for metal-air batteries, manganese oxides ( $\text{MnO}_x$ ) are a kind of the particularly interesting candidates due to their rich oxidation states, chemical compositions and crystal structures. As identified, manganese oxides have high catalytic activity for the decomposition of  $\text{H}_2\text{O}_2$  induced by the simultaneous oxidation and reduction of the surface manganese ions (i.e.,  $\text{Mn}^{4+}/\text{Mn}^{3+}$  for the mixed manganese based catalyst)<sup>19</sup>. For example,  $\text{MnO}_2$  is the most commonly used ORR electro-catalyst in commercial zinc-air batteries<sup>20</sup>. Besides  $\text{MnO}_x$ ,  $\text{Co}_3\text{O}_4$ , one of the well-known spinel materials, has also been studied for decades as a highly efficient and corrosion-resistant ORR/OER catalyst in alkaline media<sup>21</sup>. To further improve the electrochemical activity of  $\text{Co}_3\text{O}_4$  electro-catalysts, other metal atoms were also incorporated into the spinel structure to form  $\text{M}_x\text{Co}_{3-x}\text{O}_4$  ( $\text{M} = \text{Ni}/\text{Mn}/\text{Cu}/\text{Li}$ ) catalysts in which when  $\text{M} = \text{Ni}/\text{Mn}$ , the materials served as the ORR catalysts, and when  $\text{M} = \text{Cu}/\text{Mn}/\text{Li}$ , the materials as the OER catalysts<sup>22–28</sup>. Although the incorporation of these metals into  $\text{Co}_3\text{O}_4$  could increase the number of catalytically active sites<sup>6,29</sup>, the catalyst's electrical conductivity was found to be insufficient.

Recent studies reported that the combination between oxides and nano-structural carbons such as graphene and carbon nanotubes (CNTs) to form ORR catalysts could have both improved electro-catalytic activity and stability<sup>28,30,31</sup>. This could be attributed to their high conductivity, large surface area, and high electrochemical stability<sup>32–34</sup>. To the best of our knowledge, there has been no report on the combination among  $\text{MnO}_2$ ,  $\text{Co}_3\text{O}_4$  and carbon-based materials to form hybrid catalysts for improving the electro-catalytic performance of the materials in rechargeable metal-air batteries. It is expected that by combining the transition metal oxides with carbon-based material via a facile hydrothermal process would lead to a strong hybrid effect to enhance the catalytic performance. Based on this strategy, we have designed and synthesized the hybrid material via a facial two-pot method where the precursors of the metal-oxide (Mn and Co) and CNTs are justly mixed into a single reaction to produce the final catalysts.

The two-pot synthesis reported in this paper is based on a hydrothermal process, which is simple and cost effective, thus allowing highly practical and scalable preparation of the catalyst material. The synthesized novel hybrid material composed of  $\text{Co}_3\text{O}_4$  supported on  $\text{MnO}_2$  nanotubes ( $\text{Co}_3\text{O}_4/\text{MnO}_2$ ) and its CNTs hybrid (abbreviated as  $\text{Co}_3\text{O}_4/\text{MnO}_2$ -CNTs) have been explored as the bi-functional catalysts, and the tested results show that these catalysts have very high ORR/OER activities and stability. It is believed that the electro-catalytic activities of these catalysts are contributed by the novel phases of the inorganic nano-particles and their intimate to the underlying CNT networks. Using this hybrid electro-catalyst ( $\text{Co}_3\text{O}_4/\text{MnO}_2$ -CNTs) for the air cathode, a rechargeable Zn-air battery is constructed for catalyst validation. Compared to baseline catalyst, both remarkable high recharge ability and durability of a practical zinc-air battery are demonstrated by utilizing atmosphere air as the source of oxidant instead of pure purged oxygen, which are even better than the Pt/C catalyst in alkaline solutions. In particular, the significantly reduced ORR and OER over-potentials are achieved, resulting in both high battery performance (a discharge peak power density of  $450 \text{ mW cm}^{-2}$  and a current density  $324 \text{ mA cm}^{-2}$  at  $1.0 \text{ V}$  are achieved) and high durability (long cycle-life), demonstrating that this  $\text{Co}_3\text{O}_4/\text{MnO}_2$ -CNTs catalyst is also one of the most promising non-precious catalysts, particularly for the OER.

## Experiment Methods

**Synthesis of  $\text{MnO}_2$  nanotube-supported  $\text{Co}_3\text{O}_4$  and its carbon nanotube hybrid cathode catalyst.** A modified facile two-pot hydrothermal method was used to synthesize  $\text{Co}_3\text{O}_4/\text{MnO}_2$ -CNTs hybrid cathode catalyst for rechargeable zinc-air batteries. All chemicals used in this work were analytical grade and used without further purification. For a typical synthetic experiment, Solution A was synthesized by dissolving  $0.790 \text{ g}$  of  $\text{KMnO}_4$  and  $2 \text{ mL}$  of concentrated  $\text{HCl}$  (37%) in  $50 \text{ mL}$  of deionized water with stirring. Then the solution was transferred into a  $100 \text{ mL}$  Teflon-lined stainless steel autoclave and sealed and hydrothermally treated at  $140^\circ\text{C}$  for 12 hours. The collected powder of  $\text{MnO}_2$  nanotubes was treated by several centrifuge-wash cycles with ethanol and deionized water, and then dried in air at  $70^\circ\text{C}$  for 24 hours. Solution B was prepared by adding  $0.25 \text{ g}$  of  $\text{Co}(\text{NO}_3)_2 \cdot 4\text{H}_2\text{O}$  in  $30 \text{ mL}$  of  $1.3 \text{ mol L}^{-1}$  ammonia solution. Then  $0.25 \text{ g}$  as-prepared  $\text{MnO}_2$  nanotube powder made from Solution A and  $0.125 \text{ g}$  CNTs (purity > 95 wt.%, length  $\sim 15 \mu\text{m}$ , diameter  $30\text{--}50 \text{ nm}$ , Alpha Nano Technology Co. Ltd., China) were dispersed in Solution B by ultrasonication for 1 hour. This mixture was then transferred into a  $100 \text{ mL}$  autoclave, which was sealed and maintained at  $150^\circ\text{C}$  for 5 hours. The precipitate was separated by several centrifuge-wash cycles with deionized water, and then dried at  $60^\circ\text{C}$  for 6 hours. The collected powder of  $\text{Co}_3\text{O}_4/\text{MnO}_2$ -CNTs hybrid materials were calcined in air at  $400^\circ\text{C}$  for 1 hour to obtain the product. For a comparison,  $\text{MnO}_2$  nanotubes-supported hollow porous  $\text{Co}_3\text{O}_4$  nanomaterials ( $\text{Co}_3\text{O}_4/\text{MnO}_2$ ) were also prepared under the same procedure except the CNTs was not added.

**Material characterization.** X-ray diffraction (XRD) was used to identify the phase composition of synthesized  $\text{Co}_3\text{O}_4/\text{MnO}_2$ -CNTs sample over the  $2\theta$  range from  $5^\circ$  to  $80^\circ$  using a Bruker AXS D8 advance diffractometer with nickel filtered  $\text{Cu K}\alpha$  radiation ( $\lambda = 1.5406 \text{ \AA}$ ), and the energy-dispersive X-ray (EDX) spectra were taken by a JEOL JSM5600 scanning electron microscope at an accelerating voltage of  $20 \text{ kV}$ . The microstructural characteristics of  $\text{Co}_3\text{O}_4/\text{MnO}_2$ -CNTs hybrid samples were recorded by transmission electron microscopy (TEM), high-resolution transmission electron microscopy (HR-TEM, JEOL JEM-2010F) working at  $200 \text{ kV}$  accelerating voltage, and the lattice structure was identified by selected area electron diffraction (SAED) technique.

**Electrode preparation and electrochemical characterization.** A half-cell setup containing a rotating disc electrode (RDE) was used to investigate both the ORR and the OER catalytic activities of the  $\text{Co}_3\text{O}_4/\text{MnO}_2$ -CNTs catalyst samples. The working electrode was fabricated by casting Nafion<sup>®</sup>-impregnated catalyst ink onto a glassy carbon disk electrode ( $5 \text{ mm}$  in diameter). In the preparation of catalyst ink,  $10 \text{ mg}$  of the catalyst

was ultrasonically dispersed into 1 mL ethanol and 8  $\mu\text{L}$  5 wt% Nafion<sup>®</sup> solution to form a catalyst ink. Then, 5  $\mu\text{L}$  of the catalyst ink was deposited onto the disk and dried at room temperature. The working electrode was allowed to achieve a catalyst loading of 0.1 mg  $\text{cm}^{-2}$ . Electrochemical activity of the samples was studied using a linear sweep voltammetry. In the measurements, the catalyst-coated working electrode was immersed in a half-cell containing 0.1 M KOH aqueous electrolyte, in which a platinum foil and a saturated calomel electrode (SCE) were used as the counter and reference electrodes, respectively. Catalyst activities toward both ORR and OER were evaluated in oxygen-saturated electrolyte solution in a potential range from 1.67 to 0.1 V vs RHE. The rotation rate was controlled at 1600 rpm. A commercial Pt/C catalyst (30 wt% platinum on carbon, Johnson Matthey) and CNTs were used as the baselines and tested using the same procedure as that for  $\text{Co}_3\text{O}_4/\text{MnO}_2$ -CNTs catalyst.

**Single cell test.** A home-made zinc–air battery, as shown in Fig. 1a, was used to validate the practical catalyst activity and stability. The air cathode was prepared by spraying the catalyst (with a loading of 2 mg  $\text{cm}^{-2}$ ) onto a gas diffusion layer (GDL) (Toray TGP-H-090) with an exposed active area of 4.0  $\text{cm}^2$  (Fig. 1b). Briefly, 20 mg of catalyst was dispersed in 5 mL of ethanol by sonication for 30 minutes. 40  $\mu\text{L}$  of 5 wt% Nafion<sup>®</sup> solution was added followed by 1 hour of additional sonication. The catalyst mixture was then sprayed onto the GDL, and dried in an oven at 60 °C for 1 hour. The catalyst loading was controlled by calculating the weight of the GDL electrode before and after the spray coating. The electrolyte used in the zinc–air battery was 10 mL of 6 M KOH, and a polished zinc plate (purity > 99.99%, thickness: 0.3 or 1.0 mm, Shengshida Metal Mater. Co. Ltd., China) was used as the anode. The discharge polarization and power density plots were obtained using a galvanodynamic method with a current density ranging from 0 to 1000 mA. Battery testing and cycling experiments were performed using the recurrent galvanic pulse method, where one cycle was consisted of a discharging step (5~10 mA  $\text{cm}^{-2}$  for 10~30 minutes, 30~50 mA  $\text{cm}^{-2}$  for 2 hours and 100 mA  $\text{cm}^{-2}$  for 30 minutes) followed by a charging step with the same current and duration time.

For all-solid-state Zinc–Air battery, the battery is fabricated by laminating an Tokuyama A901 anion-exchange membrane (Tokuyama A901 is a major type of commercially available membrane, which exhibits high  $\text{OH}^-$  conductivity of 11.4 mS  $\text{cm}^{-1}$ , ion exchange capacity of 1.7 meq  $\text{g}^{-1}$ , and generally used as a reference for comparing membrane characteristics and fuel cell performances) between an air electrode made of the above  $\text{Co}_3\text{O}_4/\text{MnO}_2$ -CNTs catalyst-loaded gas diffusion layer (GDL) (Toray TGP-H-090) and a polished zinc plate anode. Copper (Cu) foil as a substrate is attached to the zinc electrode to ensure a good conductivity. The assembled device was pressed under a pressure of 3 MPa for 1 minute by a sheeting presser to enhance the integrity of the laminated structure.

## Results and Discussion

The morphology information for the catalysts can be seen from the TEM images shown in Fig. 1(c). This figure indicates that  $\text{MnO}_2$  nano-tubes can be successfully synthesized using the facile two-pot method (Figure S1(a)), where  $\text{MnO}_2$  nanotubes consisting of the average diameter and length of 45~65 nm and 1~2  $\mu\text{m}$ , respectively. On the surface of  $\text{MnO}_2$  nanotubes, the homogeneous  $\text{Co}_3\text{O}_4$  nano-particles with an average size of 5~10 nm are densely coated (Fig. 1(d) and Figure S1(b)). The high resolution transmission electron microscopy (HR-TEM) image of the interface between a single  $\text{MnO}_2$  nanotube and  $\text{Co}_3\text{O}_4$  nanocrystal (Fig. 1(e)) reveals fringes in multiple directions with d-spacing of 0.24 nm for cubic  $\text{Co}_3\text{O}_4$  and a lattice spacing of 0.69 nm for  $\alpha$ - $\text{MnO}_2$ . The  $\text{Co}_3\text{O}_4$  nanoparticles exhibit an ecumenical crystalline structure as confirmed by the distinct diffraction dots observed in the fast Fourier transformation (FFT) (Fig. 1(f)). Further analyzing the FFT pattern reveals the characteristic lattice spacing of 0.699 nm, 0.491 nm, 0.310 nm and 0.237 nm for the  $\text{Co}_3\text{O}_4/\text{MnO}_2$  sample, indicative of the polycrystalline nature of this material. The typical TEM images as shown in Fig. 1(g,h) confirm the successful synthesis of  $\text{Co}_3\text{O}_4/\text{MnO}_2$ -CNTs hybrid material using the simple chemical route in this work. The TEM image shows that the diameter of a  $\alpha$ - $\text{MnO}_2$  tube is about 45~65 nm, and both the length and the wall thickness are almost the same as that without CNTs junction (Fig. 1(c,d)). This strongly demonstrates that a uniform and dense coating of the  $\text{Co}_3\text{O}_4$  nanoparticles on the surface of  $\text{MnO}_2$  nanotubes can be achieved even in the presence of CNTs. Interestingly, the  $\text{Co}_3\text{O}_4$  nanoparticles seem to be in a highly “hybrid” porous structure with 3~5 nm of circular hollow centers (boxed in Fig. 1(h) and Figure S1(c)), which may be ascribed to the doping effect during the formation of  $\text{Co}_3\text{O}_4/\text{MnO}_2$ -CNTs hybrid. The cobalt oxide nanoparticles are found to mainly stay on the surface of manganese dioxide nanotubes, except for some particles deposited on CNTs’ surface (circled in Fig. 1(g)). Then, 5 nm of cobalt oxide particles could slowly reunite to about 20 nm cobalt oxide particles at 400 °C. This unique structure may lead to a high surface area per unit volume, which could create more active sites for the enhanced electro-catalytic oxygen reduction reactions (Fig. 1(h)). The HR-TEM image in Fig. 1(i) reveals that  $\text{Co}_3\text{O}_4$  nanoparticles are not only binding on the manganese dioxide surface, but also supported on carbon nanotube. More importantly, cobalt oxide crystal aggregation could result in three materials linked together. This coupling effect among  $\text{Co}_3\text{O}_4$ ,  $\text{MnO}_2$  nanotubes and CNTs may allow a better diffusion of reactants through the empty spaces between the neighboring CNTs to induce a high active material utilization<sup>35</sup>. Further from the high resolution images of  $\text{MnO}_2$  nanotubes,  $\text{Co}_3\text{O}_4$  nanocrystals and CNTs, measured by HRTEM (Fig. 1(j)), the lattice spacing of 0.69 nm of  $\alpha$ - $\text{MnO}_2$  can be assigned to the (110) plane of this material<sup>33</sup> (Joint Committee on Powder Diffraction Standards file no. 41-0141), and the lattice fringe of the (311) plane with a lattice spacing of 0.24 nm to typical  $\text{Co}_3\text{O}_4$  nanoparticles (Joint Committee on Powder Diffraction Standards file no. 76-1802). Both are in a well agreement with those of  $\text{Co}_3\text{O}_4/\text{MnO}_2$  observed in Fig. 1(e). Further analyzing the FFT pattern (Fig. 1(k)) can give more characteristic lattice spacing of 0.181 nm, 0.241 nm and 0.493 nm for the hybrid  $\text{Co}_3\text{O}_4/\text{MnO}_2$ -CNTs, which is in a good consistence with the XRD diagram discussed below.

The resulting  $\text{Co}_3\text{O}_4/\text{MnO}_2$ -CNTs sample was further characterized by energy-dispersive X-ray spectroscopy (EDS) (Fig. 1(l)). Compositional analysis of the  $\text{Co}_3\text{O}_4/\text{MnO}_2$ -CNTs gives that the CNTs, O, Mn and Co contents are 26.56, 22.35, 37.09 and 11.81 wt%, respectively, and that the C, O, Mn and Co atomic percentages (at%) are 48.7, 30.77, 14.87 and 4.42, respectively (Fig. 1(l), Inset). Based on these data, it can be calculated that the

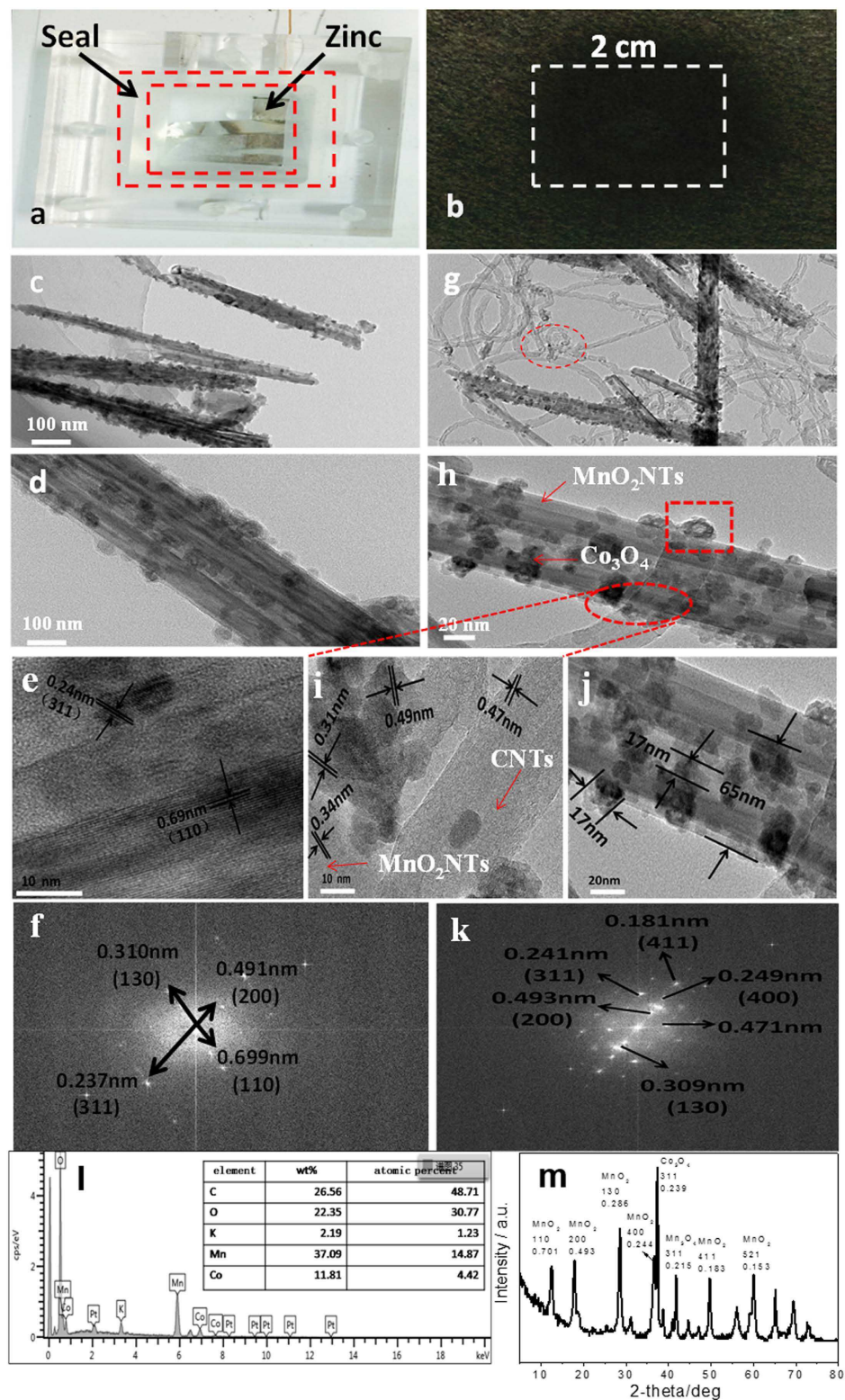


**Figure 1.** (a) Optical image of the home-made rechargeable zinc–air battery; (b) Optical image of  $\text{Co}_3\text{O}_4/\text{MnO}_2$ -CNTs hybrid catalyst-based air electrode; (c) TEM image of  $\text{Co}_3\text{O}_4/\text{MnO}_2$  hybrid material; (d) TEM image of  $\text{Co}_3\text{O}_4/\text{MnO}_2$  uniformly distributed local graph; (e) HRTEM image of the interface of  $\text{Co}_3\text{O}_4/\text{MnO}_2$  nanocrystals; (f) FFT pattern of  $\text{Co}_3\text{O}_4/\text{MnO}_2$  in the hybrid; (g) TEM image of  $\text{Co}_3\text{O}_4/\text{MnO}_2$ -CNTs hybrid catalyst; (h) TEM image of  $\text{Co}_3\text{O}_4/\text{MnO}_2$ -CNTs uniformly distributed local graph; (i) HRTEM image of the interface of  $\text{Co}_3\text{O}_4/\text{MnO}_2$ -CNTs nanocrystals; (j) HRTEM image of the  $\text{Co}_3\text{O}_4/\text{MnO}_2$ -CNTs nanocrystals; (k) FFT pattern of  $\text{Co}_3\text{O}_4/\text{MnO}_2$ -CNTs in the hybrid; (l) EDS spectrum of the  $\text{Co}_3\text{O}_4/\text{MnO}_2$ -CNTs hybrid nanomaterials (Insert: composition of the  $\text{Co}_3\text{O}_4/\text{MnO}_2$ -CNTs); (m) XRD patterns of the  $\text{Co}_3\text{O}_4/\text{MnO}_2$ -CNTs hybrid nanomaterials.

Catalysts	Crystal orientation	TEM		XRD	
		d-Spacing (nm)	2 Theta (degree)	d-Spacing (nm)	
MnO <sub>2</sub>	110	0.699	12.599	0.701	
	200	0.491	17.959	0.493	
	130	0.309	28.680	0.311	
	400	0.249	36.799	0.244	
	411	0.181	49.773	0.183	
Co <sub>3</sub> O <sub>4</sub>	311	0.239	36.991	0.239	

**Table 1.** Calculated values of d-spacing for each crystal orientation observed in the SAED pattern obtained from TEM and diffraction angles obtained from XRD of Co<sub>3</sub>O<sub>4</sub>/MnO<sub>2</sub>-CNTs.

formulas of the metal oxides match well with the Co<sub>3</sub>O<sub>4</sub> and MnO<sub>2</sub>. From the X-ray diffraction (XRD) patterns of Co<sub>3</sub>O<sub>4</sub>/MnO<sub>2</sub>-CNTs as shown in Fig. 1(m), one can see that all major diffraction peaks match well with the standard peaks of tetragonal  $\alpha$ -MnO<sub>2</sub> for the nanotube sample. For Co<sub>3</sub>O<sub>4</sub>/MnO<sub>2</sub>-CNTs hybrid material, the diffraction peaks at 12.6°, 17.9°, 28.7° and 36.7° can be indexed to (110), (200), (130) and (400) planes of MnO<sub>2</sub>, and the diffraction peak at 36.9° can be indexed to (311) plane of Co<sub>3</sub>O<sub>4</sub>, respectively. There are also some peaks that are not labelled, which are possibly related to the various intermediates that are generated in the junction (Fig. 1(m)). In addition, the d-spacing of each crystal orientation observed in the XRD pattern is also calculated based on the diffraction angle using Bragg's law, the result obtained matches closely with those calculated with the SAED pattern from the TEM characterization (as listed Table 1), confirming the successful synthesis of Co<sub>3</sub>O<sub>4</sub>/MnO<sub>2</sub>-CNTs hybrid catalyst.

The catalytic activity of the as-prepared Co<sub>3</sub>O<sub>4</sub>/MnO<sub>2</sub>-CNTs catalyst toward both ORR and OER were tested by linear sweep voltammetry (LSV) using a catalyst-coated rotating disk electrode. Figure 2(a) shows the LSV curves of as-prepared Co<sub>3</sub>O<sub>4</sub>/MnO<sub>2</sub>-CNTs hybrid in comparison with the Co<sub>3</sub>O<sub>4</sub>/MnO<sub>2</sub> one. It can be seen that on the cathodic branch, Co<sub>3</sub>O<sub>4</sub>/MnO<sub>2</sub>-CNTs exhibits a much higher ORR performance than Co<sub>3</sub>O<sub>4</sub>/MnO<sub>2</sub>, where the Co<sub>3</sub>O<sub>4</sub>/MnO<sub>2</sub>-CNTs gives an onset potential  $\sim$ 95 mV and a half-wave potential  $\sim$ 94 mV more positive than that of Co<sub>3</sub>O<sub>4</sub>/MnO<sub>2</sub>, respectively, indicating the importance of CNT injunction. The difference in half-wave potentials may be caused by a thin-film quality difference of the two samples. Further analyzing Tafel slopes (Fig. 2b) reveals that the Tafel slopes at low over potentials for Co<sub>3</sub>O<sub>4</sub>/MnO<sub>2</sub>-CNTs and Co<sub>3</sub>O<sub>4</sub>/MnO<sub>2</sub> are 113 and 195 mV per decade, respectively, suggesting the former has a much high catalytic activity than the latter. The large difference in the Tafel slopes may indicate the difference in their rate limiting steps. On the basis of the onset potentials, half-wave potentials and Tafel slopes, one can conclude that Co<sub>3</sub>O<sub>4</sub>/MnO<sub>2</sub>-CNTs hybrid catalyst is much more active than Co<sub>3</sub>O<sub>4</sub>/MnO<sub>2</sub> for the ORR. The increased ORR activity could be attributed to the beneficial effect of CNTs due to their excellent conductivity, large surface area and networking effect as discussed above (Fig. 1(h,i)). As in metal-air batteries, apart from the ORR activity of the bi-functional catalyst, the excellent OER activity is particularly critical. As shown in Fig. 2(a), Co<sub>3</sub>O<sub>4</sub>/MnO<sub>2</sub>-CNTs hybrid catalyst delivers an OER current density of 7.8 mA cm<sup>-2</sup> at 1.7 V, which is 1.6 times higher than that of Co<sub>3</sub>O<sub>4</sub>/MnO<sub>2</sub>. Similar characteristics of onset potential can also be obtained, where Co<sub>3</sub>O<sub>4</sub>/MnO<sub>2</sub>-CNTs shows a  $\sim$ 90 mV more positive than that of Co<sub>3</sub>O<sub>4</sub>/MnO<sub>2</sub> for OER (Fig. 2(a), Inset). The measured Tafel slope for Co<sub>3</sub>O<sub>4</sub>/MnO<sub>2</sub> is 85.6 mV per decade, which was greatly reduced to 61.5 mV per decade if Co<sub>3</sub>O<sub>4</sub>/MnO<sub>2</sub>-CNTs catalyst is used, indicative of superior catalytic activity of Co<sub>3</sub>O<sub>4</sub>/MnO<sub>2</sub>-CNTs hybrid to Co<sub>3</sub>O<sub>4</sub>/MnO<sub>2</sub> even for OER (Fig. 2(c)). For further comparison, Fig. 2(d) shows the linear sweep potential measurements with Co<sub>3</sub>O<sub>4</sub>/MnO<sub>2</sub>-CNTs, CNTs, Ir/C and the commercial Pt/C nanoparticles tested at the same conditions. It is encouraging to note that the Co<sub>3</sub>O<sub>4</sub>/MnO<sub>2</sub>-CNTs hybrid catalyst exhibits a high ORR onset potential of 0.958 V, which is only  $\sim$ 36 mV more negative than that of Pt/C catalyst (with an onset potential of 0.994 V), and the ORR current is also much larger than those of both CNTs and Ir/C (with an onset potential of only 0.720 V and 0.838 V, respectively). At 0.2 V, Co<sub>3</sub>O<sub>4</sub>/MnO<sub>2</sub>-CNTs can give a catalytic ORR current density of 3.8 mA cm<sup>-2</sup> along with a defined diffusion-limiting current plateau, which is slightly less than that of Pt/C catalyst (with a defined diffusion-limiting current plateau of 5.1 mA cm<sup>-2</sup>). The excellent OER activity of the Co<sub>3</sub>O<sub>4</sub>/MnO<sub>2</sub>-CNTs hybrid catalyst is further confirmed by the measured onset potential of 1.454 V, which is  $\sim$ 50 mV more negative than Pt/C catalyst,  $\sim$ 200 mV more negative than CNTs and only  $\sim$ 26 mV more positive than Ir/C. The OER current densities catalyzed by Co<sub>3</sub>O<sub>4</sub>/MnO<sub>2</sub>-CNTs, Ir/C, CNTs and Pt/C at 1.7 V are 7.9 mA cm<sup>-2</sup>, 8.0 mA cm<sup>-2</sup>, 0.4 mA cm<sup>-2</sup> and 0.9 mA cm<sup>-2</sup>, indicating that this Co<sub>3</sub>O<sub>4</sub>/MnO<sub>2</sub>-CNTs can give 20 and 8.5 times higher ORR activity than CNTs and Pt/C. It should be mentioned that for OER, the state-of-the-art catalysts are carbon-supported Ir. From Fig. 2(d), it can be seen that the Co<sub>3</sub>O<sub>4</sub>/MnO<sub>2</sub>-CNTs hybrid catalyst is close to Ir/C. These results suggest that Co<sub>3</sub>O<sub>4</sub>/MnO<sub>2</sub>-CNTs is not only an excellent ORR catalyst but also an outstanding OER catalyst. The high activities of the Co<sub>3</sub>O<sub>4</sub>/MnO<sub>2</sub>-CNTs bi-functional hybrid catalyst for both and ORR and OER suggest that the injunction of CNT may change the OER mechanism due to the unique architectures induced from the synergistic effect and the interface effect among the MnO<sub>2</sub> nanotubes, Co<sub>3</sub>O<sub>4</sub> nanoparticles and CNTs. One should emphasize that the synthesis sequence is very important for Co<sub>3</sub>O<sub>4</sub>/MnO<sub>2</sub>-CNTs hybrid formation. Unlike the two-pot method-assisted growth of MnO<sub>2</sub> nanotubes coupling with CNTs, only the aggregated Co<sub>3</sub>O<sub>4</sub> nanoparticles could be observed if the CNTs were firstly inducted into KMnO<sub>4</sub> precursor solution. No formation of MnO<sub>2</sub> nanotubes could be realized and the redundant CNTs were even "dissolved" into these particles completely (Figure S2, Supporting Information). In a further set of experiments, Fig. 2(e,f) shows the LSV curves at different loadings of as-prepared Co<sub>3</sub>O<sub>4</sub>/MnO<sub>2</sub>-CNTs catalyst. Obviously,

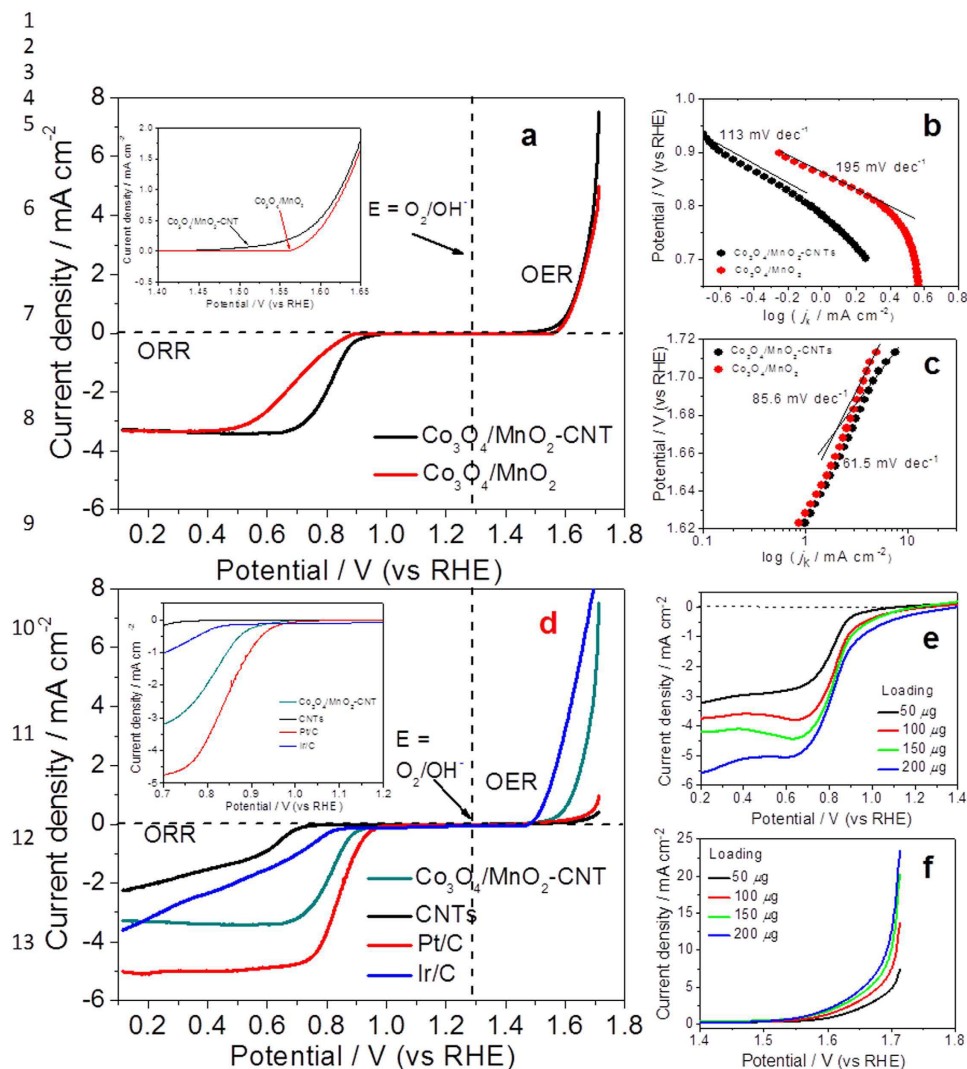


**Figure 2.** (a) ORR and OER polarization curves of  $\text{Co}_3\text{O}_4/\text{MnO}_2$  and  $\text{Co}_3\text{O}_4/\text{MnO}_2$ -CNTs (Insert: enlarged OER); (b) Tafel plots of ORR currents; (c) Tafel plots of OER currents; (d) ORR and OER polarization curves of  $\text{Co}_3\text{O}_4/\text{MnO}_2$ -CNTs, 20%Pt/C, Ir/C and CNTs (Insert: enlarged ORR); (e) ORR polarization curves catalyzed by different loadings of  $\text{Co}_3\text{O}_4/\text{MnO}_2$ -CNTs catalyst; (f) OER polarization curves catalyzed by different loadings of  $\text{Co}_3\text{O}_4/\text{MnO}_2$ -CNTs catalyst.

catalyst loading has a strong effect on its performance, that is, the higher the catalyst loading, the higher the catalytic current. Increasing the  $\text{Co}_3\text{O}_4/\text{MnO}_2$ -CNTs loading to  $200 \mu\text{g cm}^{-2}$  could contribute the onset potentials of  $\sim 100 \text{ mV}$  and  $\sim 50 \text{ mV}$  more positive than that of the lowest loading of  $50 \mu\text{g cm}^{-2}$  for ORR and OER, respectively. Furthermore, with increasing catalyst loading, the diffusion current is also increased.

To validate the catalyst,  $\text{Co}_3\text{O}_4/\text{MnO}_2$ -CNTs hybrid catalyst was used as the ORR catalyst loaded on the carbon fibre paper for a cathode of Zn-air battery (Zn foil with 0.3 mm thickness as anode and 6M KOH as the electrolyte) (Fig. 3(a)). It was observed that the assembled battery had an open circuit voltage of 1.40 V. At a cell voltage of 1.0 V, it gave a high current density of  $224 \text{ mA cm}^{-2}$ . The peak power density could be as high as  $313 \text{ mW cm}^{-2}$  at 0.66 V (Fig. 3(b)), which is significantly superior to those most recently reported Zn-air primary batteries (Table S1, Supporting Information). This  $\text{Co}_3\text{O}_4/\text{MnO}_2$ -CNTs cathode catalyst associated primary Zn-air battery was also stable in terms of the performance. When the cell was galvanostatically discharged at a current density of  $10 \text{ mA cm}^{-2}$  for 120 hours, no obvious voltage drop was observed owing to the stability of  $\text{Co}_3\text{O}_4/\text{MnO}_2$ -CNTs for ORR (Fig. 3(c)). It is worthwhile to mention that a higher practical energy density can be easily achieved by simply replenishing the metal anode or electrolyte<sup>21</sup>. To study the durability of air cathode without the failure contribution from battery anode, we tested the cell performance using a zinc plate with a thickness of 1 mm instead of 0.3 mm. Surprisingly, the cell gave a high current density of  $324 \text{ mA cm}^{-2}$  at a cell voltage of 1.0 V, and a very high peak power density in excess of  $450 \text{ mW cm}^{-2}$  at 0.7 V (Fig. 3(d)), suggesting that simply replenishing the metal anode or electrolyte could regenerate the battery for subsequent runs at the same performance level with the used  $\text{Co}_3\text{O}_4/\text{MnO}_2$ -CNTs cathode. On the contrary, the current density of  $100 \text{ mA cm}^{-2}$  was only obtained by 20% Pt/C, with a very low peak power density of  $140 \text{ mW cm}^{-2}$  at the same measuring conditions

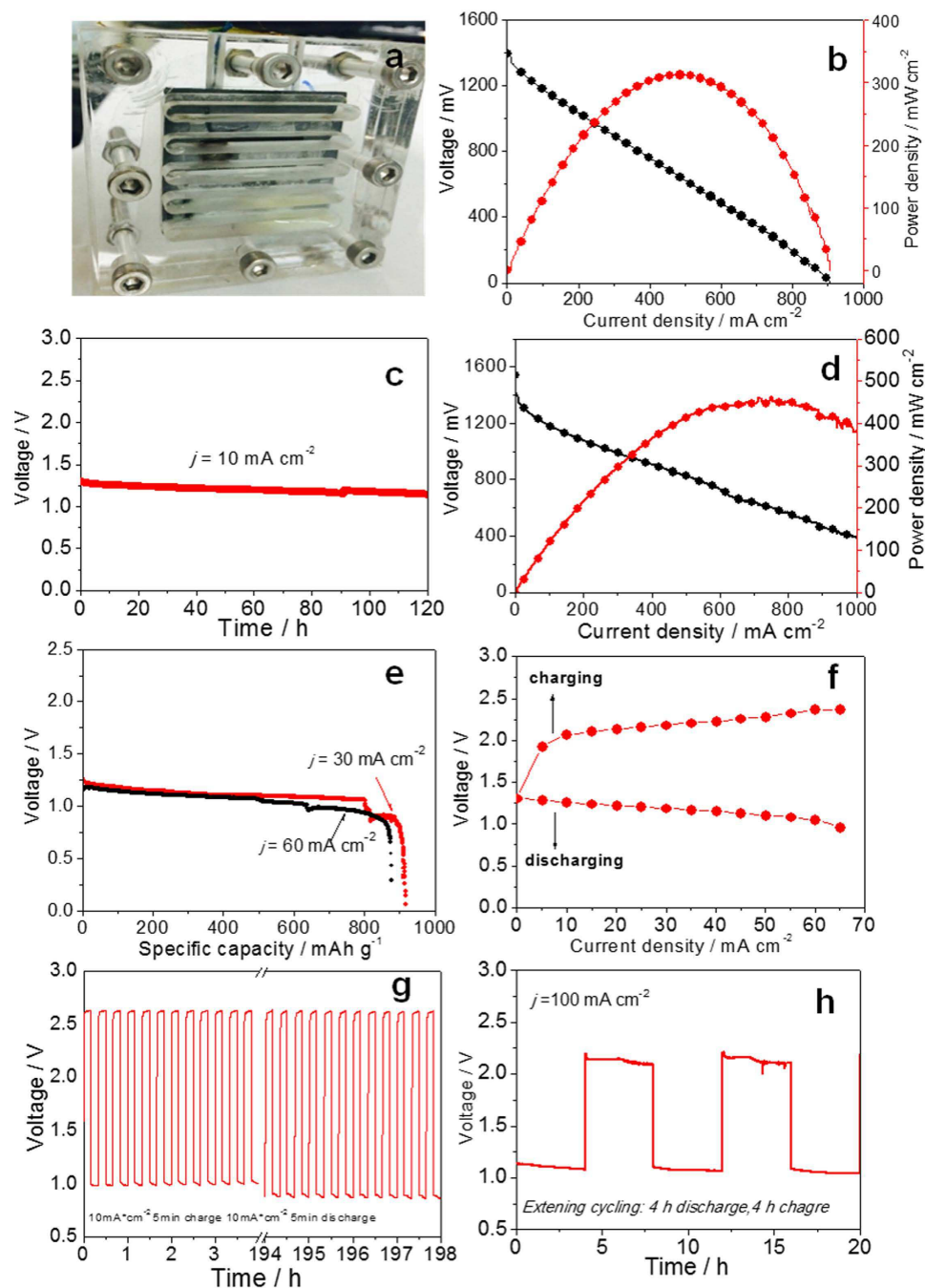


**Figure 3.** (a) Optical image of the already assembled zinc air battery; (b) Polarization curve and corresponding power density plot of the Zn-air battery using  $\text{Co}_3\text{O}_4/\text{MnO}_2\text{-CNTs}$  as the cathode catalyst, with Znic plate with a thickness of 0.3 mm as the anode; (c) Long-time discharge curve; (d) Polarization curve and corresponding power density plot of the Zn-air battery using Znic plate with a thickness of 1 mm; (e) Typical discharge curves of primary Zn-air batteries with  $\text{Co}_3\text{O}_4/\text{MnO}_2\text{-CNTs}$  as the cathode catalyst under continuous discharge until complete consumption of Zn. Specific capacity was normalized to the mass of consumed Zn. (f) Charge and discharge polarization (V-i) curves of the bi-electrode Zn-air battery; (g) Cycling data at  $10 \text{ mA cm}^{-2}$  in cycle periods of 10 minutes per cycle; (h) Cycling data at  $100 \text{ mA cm}^{-2}$  in long cycle periods in 8 hours per cycle.

(Figure S3, Supporting Information). Recently, Zn-air fuel cells or Zn-air flow batteries have been proposed and demonstrated to power electric vehicles with high power, long driving distance and commercial viability<sup>8,22,36</sup>. They could be quickly refueled with fresh metallic Zn powders (mechanical charging), and the produced zincate species in the electrolyte could be collected and recovered in off-site regeneration facilities. For a battery at  $30 \text{ mA cm}^{-2}$ , the specific capacity normalized to the mass of consumed Zn was  $\sim 907 \text{ mAh g}^{-1}$ , corresponding to a high energy density  $\sim 1000 \text{ Wh kg}^{-1}$  (Fig. 3(e)). Even for the battery at  $60 \text{ mA cm}^{-2}$ , the specific capacity normalized to the mass of consumed Zn was still  $\sim 880 \text{ mAh g}^{-1}$ , corresponding to a high energy density  $> 900 \text{ Wh kg}^{-1}$

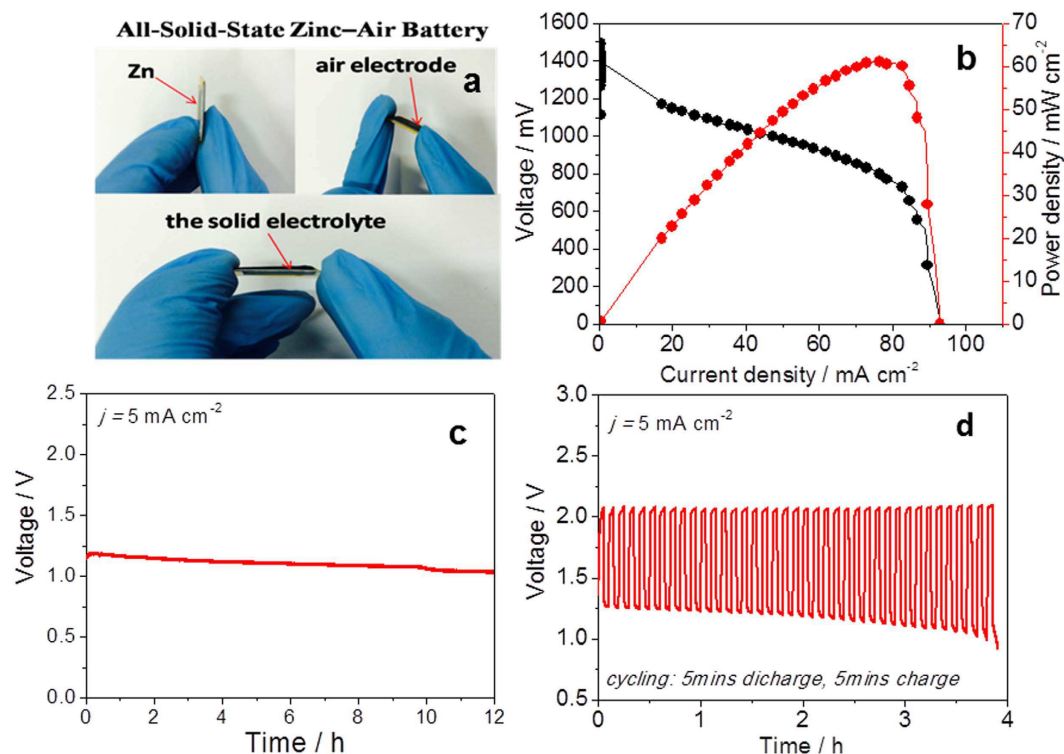


**Figure 4.** (a) A home-made all-solid-state Zinc–Air Battery; (b) Polarization curve and corresponding power density plot of the all-solid-state Zn-air battery using  $\text{Co}_3\text{O}_4/\text{MnO}_2\text{-CNTs}$  as the cathode catalyst, with Znic plate with a thickness of 0.1 mm as the anode; (c) Long-time discharge curve; (d) Cycling data at  $5 \text{ mA cm}^{-2}$  in cycle periods of 10 minutes per cycle.

(Fig. 3(e)). Our  $\text{Co}_3\text{O}_4/\text{MnO}_2\text{-CNTs}$  ORR catalyst should be ideally suited for such a refueling primary Zn-air batteries owing to the exceptional high ORR activity and durability.

Using the cathode catalyst developed in this work, an electrochemically rechargeable Zn-air battery was also constructed and tested. The  $\text{Co}_3\text{O}_4/\text{MnO}_2\text{-CNTs}$  ink was loaded onto a single cathode for a Zn-air battery for charge and discharge cycling experiments. The electrolyte used was 6 M KOH. Figure 3(f) shows the charge and discharge polarization curves of a rechargeable Zn-air battery. Under different charge and discharge current density, the charge and discharge voltages of zinc air battery have shown good performance. As shown in Fig. 3(f,g), such a battery exhibits a stable cycling stability when charged and discharged galvanostatically at controlled current densities ( $10\sim 100 \text{ mA cm}^{-2}$ ) and cycling pattern (10 minute~8 hours per charge or discharge period). It can be observed that the battery has a much better performance when the charging and discharging currents are small and the cycle time is short (for example,  $10 \text{ mA cm}^{-2}$ , 10 minutes per cycle, in Fig. 3(g)). Even using the extended cycling test (4 hours of discharge followed by 4 hours of charge at  $100 \text{ mA cm}^{-2}$ ), the battery can still show both long term durability and narrow charge–discharge voltage gap ( $\sim 1.0 \text{ V}$ ) (Fig. 3(h)). It should be noted that the battery oxidant feeding was by an un-enforced atmosphere air instead of pure oxygen or enforced air flow. The results described above are significantly improved over previous reports on Zn-air primary batteries, where oxygen (99.6%) was continuously fed to the cathode during the measurements using 0.2M zinc acetate as electrolyte or the zinc plate being replaced for every certain cycles (Table S2, Supporting Information)<sup>21,36</sup>.

As is known, zinc–air batteries mostly operate in alkaline media, such as 6 M KOH, for the sake of higher activity of both the zinc electrode and air electrode. However, the side-reaction products of  $\text{K}_2\text{CO}_3$  or  $\text{KHCO}_3$ , induced by the  $\text{CO}_2$  in air, can result in the carbon precipitation problem for zinc–air batteries. Moreover, for open systems as zinc–air batteries, water volatilization from the liquid electrolytes is an important cause of performance attenuation. Other issues such as electrolyte leakage and low safety are still the challenges for liquid electrolyte-based metal–air batteries. It has been proposed and evaluated that solid electrolyte can help minimize above challenges<sup>37</sup>. They are also able to suppress the self-corrosion of zinc and eliminate its carbonation. Moreover, using both thin film electrode and polymer electrolyte design can facilitate the physical flexibility of zinc–air batteries, providing remarkable advantages over currently available battery options, and may result in a complete redesign of modern electronics particularly for emerging portable and flexible applications. Figure 4(a) shows a fabrication process of the all-solid-state zinc air battery assembly, where the catalyst is loaded on the carbon fibre paper for a cathode, Zn foil with 0.03 mm thickness as the anode, and the Tokuyama membrane as solid electrolyte. The assembled battery shows an open circuit voltage of 1.40 V. Additionally, at a cell voltage of 1.0 V, the cell exhibits a high current density of  $100 \text{ mA cm}^{-2}$ , and the peak power density of  $62 \text{ mW cm}^{-2}$  (Fig. 4(b)). When the battery is galvanostatically discharged at a current density of  $5 \text{ mA cm}^{-2}$  for 12 hours, no obvious voltage drop can be observed owing to the stability of  $\text{Co}_3\text{O}_4/\text{MnO}_2\text{-CNTs}$  for ORR (Fig. 4(c)). Surprisingly, further

for the charge and discharge cycling experiments, the discharge (2.125 V) and charge potentials (1.25 V) under the all-solid-state condition remain virtually unchanged during the overall cycles, which is similar to the one with liquid electrolyte. From Fig. 4(d), it can be seen that the battery shows a very good stability in terms of charging. Such a battery exhibits a stable cycling stability when charged and discharged galvanostatically at controlled current densities ( $5 \text{ mA cm}^{-2}$ ) and cycling pattern (5 minutes per charge or discharge period). Compared with the potential of the charging, only minuscule changes for discharge potentials are observed at last several cycles. The observed potential changes could be due to the delamination of cell components. At this region, the Zn foil was found to be gradually thicken, and more soluble zinc salts were accumulated inside the electrolyte and the Zinc foil. In spite of this, the fabricated all-solid-state cell exhibits stable cycle performance. After 4 hours (24 cycles) operating, the cell voltage is still maintained above 1 V, demonstrating a linear charge–discharge voltage profile. The superior cycling stability and recharge ability of this all-solid-state cell can be attributed to its highly flexible components along with structural integrity between the electrodes and the membrane, and also the improved catalytic activities during the oxygen reactions due to a very strong synergy between  $\text{Co}_3\text{O}_4/\text{MnO}_2$  and NCNT species. A high volumetric energy density (based on the zinc foil volume) corresponding to a gravimetric energy density (based on the zinc foil mass) can be achieved to be  $2891 \text{ Wh L}^{-1}$  and  $597 \text{ Wh kg}^{-1}$ , respectively. These results are almost 4 times higher than the reported high-energy-density all-solid-state lithium-ion batteries ( $152 \text{ mAh g}^{-1}$ )<sup>38</sup> and Zn– $\text{MnO}_2$  batteries ( $308 \text{ mAh g}^{-1}$ )<sup>39</sup>, demonstrating the advancement of such a  $\text{Co}_3\text{O}_4/\text{MnO}_2$ -CNTs catalyst-based all-state Zinc-air battery over other devices reported.

## Conclusions

In summary, a  $\text{MnO}_2$  nanotubes-supported  $\text{Co}_3\text{O}_4$  ( $\text{Co}_3\text{O}_4/\text{MnO}_2$ ) material and its composite with CNTs ( $\text{Co}_3\text{O}_4/\text{MnO}_2$ -CNTs) are successfully synthesized through a facile two-pot precipitation reaction and hydrothermal process. This  $\text{Co}_3\text{O}_4/\text{MnO}_2$ -CNTs hybrid nanocatalyst is used as a highly active bi-functional catalyst for the oxygen reduction and oxygen evolution reactions in both primary and secondary Zn-air batteries. Experiments show that this bifunctional catalyst has both higher catalytic ORR and OER activities and stability than other baseline materials such as  $\alpha$ - $\text{MnO}_2$  nanotubes, CNTs and even commercially available Pt/C catalysts. The high performance of this novel catalyst is believed to be induced by the hybrid effect among  $\text{MnO}_2$  nanotubes,  $\text{Co}_3\text{O}_4$  and CNTs, which can produce a synergy for enhancing its both catalytic ORR and OER activities and stability. To validate this catalyst material, both primary and electrochemically rechargeable Zn-air batteries are employed, in which  $\text{Co}_3\text{O}_4/\text{MnO}_2$ -CNTs is used as the cathode (or positive electrode) catalyst. Particularly, the rechargeable battery shows the high performance with an excellent cycling stability. The maximum power density achieved can be as high as  $450 \text{ mW cm}^{-2}$ . In addition, benefiting from the use of highly flexible electrodes and polymer electrolyte membrane, the rechargeable Zn-air battery can also be fabricated into all-solid-state one through a simple solid-state approach, which exhibits both excellent peak power density and cyclic stability. All of these battery tests have confirmed that this  $\text{Co}_3\text{O}_4/\text{MnO}_2$ -CNTs bifunctional catalyst developed in this work has a significant advantage over existing commercial bifunctional catalysts in practical Zn-air batteries.

## References

- Armand, M. & Tarascon, J. M. Building better batteries. *Nature* **451**, 652–657 (2008).
- Arico, A. S., Bruce, P., Scrosati, B., Tarascon, J. M. & Schalkwijk, W. V. Nanostructured Materials for Advanced Energy Conversion and Storage Devices. *Nat. Mater.* **4**, 366–377 (2005).
- Liu, R. S., Zhang, L., Liu, H., Sun, A. & Zhang, J. *Electrochemical Technologies for Energy Storage and Conversion Vol. 2* (Wiley-VCH, Weinheim, Germany, 2012).
- Girishkumar, G., McCloskey, B., Luntz, A. C., Swanson, S. & Wilcke, W. Lithium-air battery: promise and challenges. *J. Phys. Chem. Lett.* **1**, 2193–2203 (2010).
- Scrosati, B., Hassoun, J. & Sun, Y. K. Lithium-ion batteries, A look into the future. *Energy Environ. Sci.* **4**, 3287–3295 (2011).
- Lee, D. U., Kim, B. J. & Chen, Z. W. One-pot synthesis of a mesoporous  $\text{NiCo}_2\text{O}_4$  nanoplatelet and graphene hybrid and its oxygen reduction and evolution activities as an efficient bi-functional electrocatalyst. *J. Mater. Chem. A* **1**, 4754–4762 (2013).
- F. Cheng & J. Chen, Metal–Air Batteries: from Oxygen Reduction Electrochemistry to Cathode Catalysts. *Chem. Soc. Rev.* **41**, 2172–2192 (2012).
- Chen, Z. *et al.* Highly Active and Durable Core–Corona Structured Bifunctional Catalyst for Rechargeable Metal–Air Battery Application. *Nano. Lett.* **12**, 1946–1952 (2012).
- Rahman, M. A., Wang, X. & Wen, C. High Energy Density Metal–Air Batteries: A Review. *J. Electrochem. Soc.* **160**, 1759–1771 (2013).
- Cao, R., Lee, J., Liu, M. & Cho, J. Recent Progress in Non-Precious Catalysts for Metal–Air Batteries. *Adv. Energy Mater.* **2**, 816–829 (2012).
- Chervin, C. N. *et al.* Redesigning air cathodes for metal–air batteries using  $\text{MnO}_x$ -functionalized carbon nanofoam architectures. *J. Power Sources* **207**, 191–198 (2012).
- Guo, S., Dong, S. & Wang, E. Nitrogen-Doped Carbon Nanotubes as Platinum Catalyst Supports for Oxygen Reduction Reaction in Proton Exchange Membrane Fuel Cells. *ACS Nano* **4**, 547–555 (2009).
- Bing, Y. H., Liu, H. S., Zhang, L., Ghosh, D. & Zhang, J. J. NiPt hollow nanocatalyst: Green synthesis, size control and electrocatalysis. *Chem. Soc. Rev.* **39**, 2184–2202 (2010).
- Hoque, M. *et al.* Multigrain Platinum Nanowires Consisting of Oriented Nanoparticles Anchored on Sulfur-Doped Graphene as a Highly Active and Durable Oxygen Reduction Electrocatalyst. *Adv. Mater.* **27**, 1229–1234 (2015).
- Seo, M. H., Choi, S. M., Kim, H. J. & Kim, W. B. The graphene-supported Pd and Pt catalysts for highly active oxygen reduction reaction in an alkaline condition. *Electrochem. Commun.* **13**, 182–185 (2011).
- Lim, E. J. *et al.* Highly dispersed Ag nanoparticles on nanosheets of reduced graphene oxide for oxygen reduction reaction in alkaline media. *Electrochem. Commun.* **28**, 100–103 (2013).
- Wang, F. B., Wang, J., Shao, L., Zhao, Y. & Xia, X. H. Hybrids of gold nanoparticles highly dispersed on graphene for the oxygen reduction reaction. *Electrochem. Commun.* **38**, 82–85 (2014).
- Liang, Y. *et al.* Covalent hybrid of spinel manganese-cobalt oxide and graphene as advanced oxygen reduction electrocatalysts. *J. Am. Chem. Soc.* **134**, 3517–3523 (2012).
- Li, Y. & Dai, H. J. Recent advances in zinc-air batteries. *Chem. Soc. Rev.* **43**, 5257–5275 (2014).

20. Neburchilov, V., Wang, H. J., Martin, J. J. & Qu, W. A review on air cathodes for zinc–air fuel cells. *J. Power Sources* **195**, 1271–1291 (2010).
21. Li, Y. *et al.* Advanced zinc–air batteries based on high-performance hybrid electrocatalysts. *Nat. Commun.* **4**, 1805–1812 (2013).
22. Li, J., Xiong, S., Li, X. & Qian, Y. A facile route to Synthesize Multiporous  $\text{MnCo}_2\text{O}_4$  and  $\text{CoMn}_2\text{O}_4$  Spinel Quasi-Hollow Spheres with Improved Lithium Storage Properties. *Nanoscale* **5**, 2045–2054 (2013).
23. Hamdani, M., Singh, R. N. & Chartier, P.  $\text{Co}_3\text{O}_4$  and Co-based spinel oxides bifunctional oxygen electrodes. *J. Electrochem. Sci.* **5**, 556–577 (2010).
24. Cheng, F. *et al.* Rapid room-temperature synthesis of nanocrystallinespinels as oxygen reduction and evolution electrocatalysts. *Nat. Chem.* **3**, 79–84 (2011).
25. Liang, Y. Y. *et al.*  $\text{Co}_3\text{O}_4$  nanocrystals on graphene as a synergistic catalyst for oxygen reduction reaction. *Nat. Mater.* **10**, 780–786 (2011).
26. Wang, L. *et al.*  $\text{CoMn}_2\text{O}_4$  Spinel Nanoparticles Grown on Graphene as Bifunctional Catalyst for Lithium-Air Batteries. *J. Electrochem. Soc.* **158**, 1379–1382 (2011).
27. Yuan, X. Z., Qu, W. & Fahlman J. Spinel  $\text{Ni}_x\text{Co}_{2-x}\text{O}_4$  as a Bifunctional Air Electrode for Zinc Air Batteries, *ECS Trans.* **45**, 105–112 (2013).
28. Nikolov, I. *et al.* Electrocatalytic activity of spinel related cobalties  $\text{MxCo}_{3-x}\text{O}_4$  ( $\text{M} = \text{Li, Ni, Cu}$ ) in the oxygen evolution reaction. *J. Electroanal. Chem.* **429**, 157–168 (1997).
29. Nissinen, T., Valo, T., Gasik, M., Rantanen, J. & Lampinen, M. Microwave Synthesis of Catalyst Spinel  $\text{MnCo}_2\text{O}_4$  for Alkaline Fuel Cell. *J. Power Sources* **106**, 109–115 (2002).
30. Zhang, B., Wen, Z., Ci, S., Mao, S., Chen, J. & He, Z. Synthesizing Nitrogen-Doped Activated Carbon and Probing its Active Sites for Oxygen Reduction Reaction in Microbial Fuel Cells. *ACS Appl. Mater. Interfaces* **6**, 7464–7470 (2014).
31. Fu, X. G. *et al.* Efficient Oxygen Reduction Electrocatalyst Based on Edge-Nitrogen-Rich Graphene Nanoplatelets: Toward a Large-Scale Synthesis. *ACS Appl. Mater. Interfaces* **6**, 3930–3936 (2014).
32. Wang, H. & Dai, H. J. Strongly Coupled Inorganic-Nano-Carbon Hybrid Materials for Energy Storage. *Chem. Soc. Rev.* **42**, 3088–3113 (2013).
33. Luo, J. *et al.* Synthesis of Single-Crystal Tetragonal  $\alpha\text{-MnO}_2$  Nanotubes. *J. Phys. Chem. C* **112**, 12594–12598 (2008).
34. Du, G. J. *et al.*  $\text{Co}_3\text{O}_4$  nanoparticle-modified  $\text{MnO}_2$  nanotube bifunctional oxygen cathode catalysts for rechargeable zinc-air batteries. *Nanoscale*, **5**, 4657–4661 (2013).
35. Li, Y. G., Tan, B. & Wu, Y. Y. Graphene-Wrapped  $\text{Fe}_3\text{O}_4$  Anode Material with Improved Reversible. *Nano Lett.* **8**, 265–270 (2008).
36. Lee, D. U., Choi, J. Y., Park, H. W. & Chen, Z. W. Advanced Extremely Durable 3D Bifunctional Air Electrodes for Rechargeable Zinc-Air Batteries. *Adv. Energy Mater.* **4**, 816–882 (2014).
37. Fu, J. *et al.* Flexible High-Energy Polymer-Electrolyte-Based Rechargeable Zinc–Air Batteries. *Adv. Mater.* **4**, 5617–5623 (2015).
38. Cheng, Q. *et al.* Folding Paper-Based Lithium-Ion Batteries for Higher Areal Energy Densities. *Nano Lett.* **13**, 4969–4974 (2013).
39. Wang, Z., Wu, Z., Bramnik, N. & Mitra, S. Fabrication of high-performance flexible alkaline batteries by implementing multiwalled carbon nanotubes and copolymer separator. *Adv. Mater.* **26**, 970–976 (2014).

## Acknowledgements

This work was financially supported by the National Natural Science Foundation of China (U1510120, 11202124), the International Academic Cooperation and Exchange Program of Shanghai Science and Technology Committee (14520721900), the Project of Introducing Overseas Intelligence High Education of China (2016) and the Graduate Thesis Innovation Foundation of Donghua University (EG2016034). All the financial supports are gratefully acknowledged.

## Author Contributions

J.L.Q. designed the experiment. N.N.X., X.Z. and X.M.L. conducted the experiments or draw the figures in this article. Y.Y.L., A.J.L. and J.J.Z. carried out data analysis and provided the electrochemical techniques for the research on the cycling stability of the electrodes, and they have made great work on the modification on the revision.

## Additional Information

**Supplementary information** accompanies this paper at <http://www.nature.com/srep>

**Competing financial interests:** The authors declare no competing financial interests.

**How to cite this article:** Xu, N. *et al.* Self-assembly formation of Bi-functional  $\text{Co}_3\text{O}_4/\text{MnO}_2$ -CNTs hybrid catalysts for achieving both high energy/power density and cyclic ability of rechargeable zinc-air battery. *Sci. Rep.* **6**, 33590; doi: 10.1038/srep33590 (2016).



This work is licensed under a Creative Commons Attribution 4.0 International License. The images or other third party material in this article are included in the article's Creative Commons license, unless indicated otherwise in the credit line; if the material is not included under the Creative Commons license, users will need to obtain permission from the license holder to reproduce the material. To view a copy of this license, visit <http://creativecommons.org/licenses/by/4.0/>

© The Author(s) 2016